Quantitative spatiotemporal analysis of amyloid β-induced calcium elevations in primary culture of astrocytes

Kaito Nakata

Doctor of Philosophy

The Graduate University for Advanced Studies,

SOKENDAI

School of Life Science

Department of Physiological Sciences

National Institute for Physiological Sciences

Division of Biophotonics

INDEX

Summary

Alzheimer's disease (AD) is known as a progressive neurodegenerative disorder that causes cognitive decline. Uncovering the mechanisms of neurodegeneration in the early-stage is important for establishing treatment for AD. The most pathological features of AD are known as accumulation of amyloid-β (Aβ) protein, a 40–43 amino acids peptide, in brain (Chen *et al.* 2017). Aβ aggregates into various types of assemblies, including oligomers, fibrils and senile plaque. Among these, Aβ oligomers have been known to induce neurotoxicity and hyperactivation of astrocytes. Also, Aβ oligomers have reported to induce abnormal intracellular free Ca^{2+} ($[Ca^{2+}]_i$) elevations in astrocytes (Talantova *et al*. 2013). The $[Ca^{2+}]_i$ elevations trigger excessive glutamate release from the astrocytes to the surrounding synapses. Excessive glutamate levels may induce dendritic spine loss and finally neurodegeneration. However, the signaling mechanisms of glutamate release underlying Aβ oligomers are poorly understood.

Spatial and temporal patterns vary from microdomains to astrocytes network and from sub-second to sub-minute scales in the physiological conditions (Semyanov *et al*., 2020). These patterns of $[Ca^{2+}]_i$ elevation are thought to correlate with astrocytic functions such as glutamate release (Bazargani and Attwell 2016, Santello *et al.*, 2011). However, the temporal resolutions (~1 Hz) of previous Ca^{2+} imaging under Aβ oligomers in astrocytes (Pham *et al.* 2021, Shah *et al.* 2022) were not sufficient to evaluate spatial and temporal patterns of $[Ca^{2+}]_i$ elevation. Thus, it was necessary to quantitatively evaluate the patterns of $[Ca^{2+}]_i$ elevation under Aβ oligomers utilizing high-speed imaging techniques.

In this study, to clarify the effects of Aβ oligomers on diverse $[Ca^{2+}]_i$ elevations such as fast-microdomain $[Ca^{2+}]_i$ elevations in astrocytes, I examined Aβ dimers-induced changes in the spatiotemporal patterns of $[Ca^{2+}]_i$ elevations in cultured astrocytes utilizing fast-imaging technique; two-photon excitation spinning-disk confocal microscopy.

Firstly, I observed spatial and temporal $[Ca^{2+}]_i$ patterns in primary cultured astrocytes expressing a

genetically encoded Ca^{2+} probe, GCaMP6f, in the cytosol at 10 Hz. I found that $[Ca^{2+}]_i$ elevations were composed of distinct spatial and temporal patterns. To quantitatively analyze the spatial and temporal $[Ca^{2+}]_i$ elevations, I utilized an event-based machine-learning model, the Astrocyte Quantification Analysis (AQuA) algorithm. This analysis for spontaneous astrocytic $[Ca^{2+}]_i$ elevations showed that 50% of astrocytic $[Ca^{2+}]_i$ elevations had duration time 0.5 seconds or less, and that 50% of $[Ca^{2+}]_i$ elevations had the size of $[Ca^{2+}]_i$ elevation area 35 μm^2 or less. Based on the results, I classified the patterns of $[Ca^{2+}]_i$ elevation into four categories as fast-microdomain (≤0.5 seconds, ≤35 μm^2), slow-microdomain (>0.5 seconds, ≤35 μm^2), fast-region (≤0.5 seconds, >35 μm^2) and slow-region (>0.5 seconds, >35 μm^2).

Next, I investigated quantitative relationships between Aβ dimers exposure and spatial and temporal $[Ca^{2+}]_i$ elevations. The $[Ca^{2+}]_i$ elevations were examined at concentrations of 50 nM, 200 nM, 500 nM, 2 μM, and 5 μM respectively, as referenced to previous studies (Pham *et al.* 2021, Shah *et al.* 2022). Lower doses of Aβ dimers (50, 200 nM) had no significant effect on any spatial and temporal patterns of $[Ca^{2+}]_i$ elevation. On the other hand, higher concentrations (above 500 nM) of Aβ dimers significantly increased the frequency of fast, slow-microdomain, and slow-region $[Ca^{2+}]_i$ elevations. I found that $[Ca^{2+}]_i$ elevations could be detected in response to over 500 nM Aβ dimers and the frequency and amplitude of $[Ca^{2+}]_i$ elevations were increased with greater in amount. The increase in amplitude under high concentrations of Aβ dimers may be a result of the superposition of fast, slow-microdomain, and slow-region $[Ca^{2+}]_i$ elevations.

Finally, I explored the signaling pathways of Aβ dimers-induced fast-microdomain $[Ca^{2+}]_i$ elevations. Under physiological conditions, fast-microdomain $[Ca^{2+}]_i$ elevations in astrocytes are mediated through purinergic G-protein coupled receptors (P2Y1 receptors) (Santello *et al.*, 2011). To investigate whether Aβ dimers-induced $[Ca^{2+}]_i$ elevations are mediated through P2Y1 receptors, I analyzed $[Ca^{2+}]_i$ elevations in the presence of a P2Y1 receptor antagonist (MRS2179). The frequency and amplitude of

the $[Ca^{2+}]_i$ elevations were not changed before and after treatment. Given that the activation of P2Y1 receptors leads to Ca^{2+} release from the endoplasmic reticulum (ER) via inositol trisphosphate (IP_3) receptors, it is likely that the fast, slow-microdomain and slow-region $[Ca^{2+}]_i$ elevations are due to Ca^{2+} release from the ER.

In conclusion, I revealed that the frequency of fast, slow-microdomain, and slow-region $[Ca^{2+}]_i$ elevations was increased by over 500 nM Aβ dimers exposure. Aβ dimers-induced $[Ca^{2+}]_i$ elevations might be mediated through P2Y1 receptors. These results suggest the existence of an unrecognized signaling mechanism of Aβ oligomers. Aβ dimers-induced fast-microdomain $[Ca^{2+}]_i$ elevations may modulate glutamate release. Fast-microdomain $[Ca^{2+}]_i$ elevations in astrocytes are a key signaling mechanism of glutamate release in the early-stage of AD.

Introduction

Alzheimer's disease

Alzheimer's disease (AD) is a progressive neurodegenerative disorder marked by behavior and cognitive impairment. The most striking pathological features of AD are lesions known as accumulated amyloid-β (Aβ) protein, a peptide comprising 40–43 amino acids, in the brain (Chen et al., 2017). Aβ aggregates into various types of assemblies, including oligomers, fibrils, and senile plaque. Aβ oligomers have been known to induce neurotoxicity and abnormal intracellular free Ca^{2+} ($[Ca^{2+}]_i$) elevations in astrocytes (Talantova et al., 2013). These $[Ca^{2+}]_i$ elevations might trigger excessive glutamate release from the astrocytes to the surrounding synapses, and excessive glutamate levels may induce dendritic spine loss and finally neurodegeneration (Talantova et al., 2013). Nevertheless, the cellular mechanisms of $[Ca^{2+}]_i$ elevations underlying the exposure to Aβ oligomers are not completely understood.

Astrocytes

Astrocytes, a major type of glial cells in the central nervous system, regulate synaptic transmission, remove waste products from the brain, and deliver energy fuels to neurons (Ben Haim and Rowitch, 2016; Ding et al., 2022). Through glutamate uptake from the tripartite synapse consisting of pre-, post-synapse, and perisynaptic astrocytic processes, astrocytes play a vital role in preventing glutamate excitotoxicity (Rose et al., 2018). On the basis of recent studies, researchers suggest that astrocytes also release glutamate, which is involved in the regulation of neuronal activity (Cuellar-Santoyo et al., 2023). These activities are encoded by $[Ca^{2+}]_i$ elevations in the astrocyte (Bazargani and Attwell, 2016). Spatial and temporal patterns vary from microdomains to the astrocyte network and from sub-second to sub-minute scales under physiological conditions (Semyanov et al., 2020). Recent studies have reported that fast-microdomain $[Ca^{2+}]_i$ elevations induce glutamate release, which modulates synaptic

function. Thus, fast-microdomain $[Ca^{2+}]_i$ elevations in astrocytes have become an important aspect of understanding the molecular mechanisms of neuronal functions.

Aβ oligomers-induced $[Ca^{2+}]_i$ elevations in astrocytes

Previous studies have reported that Aβ oligomers increase relatively long time-scale (from tens of seconds to several minutes) $[Ca^{2+}]_i$ elevations at the cell-size level *in vivo* and in cultured astrocytes (Shah et al., 2022.; Pham et al., 2021). It is reported that these $[Ca^{2+}]_i$ elevations involve the activation of ryanodine receptor (RyR), inositol 1,4,5-trisphosphate receptor (IP3R) expressed ER membrane or α7 nicotinic acetylcholine receptor, transient receptor potential A1 channel expressed on cell membrane (Paumier et al., 2021; Alberdi et al., 2013; Talantova et al., 2013; Pham et al., 2021). However, the effects of Aβ oligomers on localized fast $[Ca^{2+}]_i$ elevations have not been investigated.

Two-photon excitation spinning disk confocal microscopy

Fluorescence microscopy has been vital for visualizing Ca^{2+} responses in living cells by fluorescence indicators expressed genetically or loaded intracellularly. Generally, conventional fluorescence microscopy, including confocal microscopy, utilizes a single photon excitation process, achieved by absorption of a single photon, to excite fluorescent indicators by illuminating them with mainly visible wavelengths (390-700 nm). In contrast, two-photon excitation laser scanning microscopy (TPLSM) utilizes a two-photon excitation process that occurs when two photons of approximately twice the wavelength and half the energy of the light. This microscopy can acquire images with low photobleaching and phototoxicity because fluorophores are excited by near-infrared ultrashort laser pulses only within the focal volume of the objective (Lakowicz, 2006).

As for the laser scanning methods, there are two types: single-point and multi-point scanning. In single-point scanning, a single spot of the laser light beam is used for scanning in two dimensions

using a galvanometer mirror or resonant scanning to excite the fluorescence molecule in the specimen. A point detection device like a photomultiplier tube usually collects fluorescent photons returning from the focal point in a point-by-point manner. A time series of the fluorescent signal obtained in a single point scanning is reconstructed to a single fluorescent image. This scheme leads to one of the disadvantages, which is the limitation in the temporal resolution: a more extended time is required to obtain a single fluorescent image. In the case of multi-point scanning, a microlens-array disc splits the excitation laser light beam into multiple points at the focal plane; the entire field of view is scanned by those spots simultaneously. The two-dimensional tomographic images are directly projected onto the imaging plane of the two-dimensional imaging device such as charge coupled devices (CCD) camera or complementary metal oxide semiconductor (CMOS) camera. This scanning system provides the advantage of a faster frame acquisition rate (Ichihara et al., 1996).

Based on the idea that the integration of multipoint scanning technology with TPLSM could establish a novel imaging methodology, our laboratory has developed two-photon excitation spinning disk confocal microscopy (Otomo et al., 2015). The spinning disk composed of a microlens-array disk and a pinhole-array (Nikpow) disk provided the confocality into laser scanning microscopy, especially the axial spatial resolution was superior to that of the conventional TPLSM systems. Recently, we successfully visualized biological samples in a minimally invasive and high-speed manner by utilizing this microscopic technique (Kamada et al., 2022).

Outline of the research

I quantitatively analyzed $[Ca^{2+}]_i$ elevations induced by Aβ dimers in primary cultured astrocytes by a high-speed imaging technique, two-photon excitation spinning-disk confocal microscopy (Otomo et al., 2015; Otomo et al., 2020; Kamada et al., 2022). As Aβ dimers have been reported to specifically impair synapse structures (Shankar et al., 2008), I investigated the effects of Aβ dimers on $[Ca^{2+}]_i$

elevations in astrocytes. I found that low doses of Aβ dimers (50, 200 nM) exerted no significant effects on the spatial and temporal patterns of $[Ca^{2+}]_i$ elevations, whereas higher concentrations (>500 nM) of Aβ dimers significantly increased the frequency of $[Ca^{2+}]_i$ elevations and event occupancy relative to cell area. High concentrations of Aβ dimers (5 μM) further increased the amplitude of the widespread $[Ca^{2+}]_i$ elevations. These $[Ca^{2+}]_i$ elevations were inhibited by a metabotropic purinergic (P2Y1) receptor antagonist. My findings suggest that Aβ dimer-induced changes in astrocytic $[Ca^{2+}]_i$ are a key cellular mechanism in the early stages of AD.

Materials and methods

Animals

C57BL6J/Jms Slc mice (Japan SLC) were housed at 22°C–24°C with a standard 12-h light–dark cycle and ad libitum access to water and standard chow. All animal experiments were conducted according to ARRIVE guidelines, and all animal care and experimental procedures were approved by the Institutional Animal Care and Use Committee of the National Institute of Natural Sciences and were performed according to the guidelines of the National Institute for Physiological Science (Approval 23A062).

Preparation of primary cultured astrocytes and viral transfection

Primary cultures of astrocytes were prepared from the cortex of postnatal 0–3 days C57BL6J/Jms Slc mouse of either sex according to a previously published protocol (Kawano et al., 2017). Astrocytes were plated in a 75-cm^2 cell culture flask in plating medium composed of Dulbecco's modified Eagle's medium with GlutaMAX, pyruvate (35050, GIBCO), supplemented with 10% fetal bovine serum (10437, Invitrogen), 0.1% MITO + Serum Extender (355006, BD Biosciences), and penicillin, and cultured at 37°C in humidified 5% CO_2 atmosphere for 8–10 days. Growing cells were trypsinized and seeded at 3×10^3 cells/cm^2 per 9.5-mm multi-well glass bottom dish (D141400, Matsunami) coated with fibronectin (F0895, Sigma-Aldrich). Aliquots (1 μL) of adeno-associated virus (AAV) (AAV5-GfaABC1D-cyto-GCaMP6f, addgene) were inoculated onto cultured astrocytes on Days 9–11 of culture. The titer of all AAVs was more than 7.0×10^{12} genome copies/mL. The infected astrocytes were cultured for an additional 7–10 days. The culture medium was changed to artificial cerebrospinal fluid (ACSF) consisting of 146 mM NaCl, 2.5 mM KCl, 1 mM $CaCl_2$, 4 mM NaOH, 1 mM $MgCl_2$, 20 mM d-glucose, 20 mM sucrose, and 10 mM HEPES for at least 2 h before imaging. The ACSF was adjusted to pH 7.4 and 340 mOsm.

Preparation of Aβ dimers

Synthetic Aβ (1-40) S26C dimers ([AβS26C]2) were purchased from JPT Peptide Technologies (SP-Ab-24_0.5). They were used for dimerization via a disulfide bond. For experiments, the Aβ dimers were dissolved in dimethylsulfoxide (DMSO) to a concentration of 1 mM and diluted in ACSF. The final DMSO concentration was <0.5% in ACSF.

High-speed intracellular Ca^{2+} imaging

Astrocytic $[Ca^{2+}]_i$ elevations were visualized using a two-photon excitation spinning-disk confocal microscopy system (Otomo et al., 2015; Otomo et al., 2020) composed of a Ti-Sa laser light source (MaiTai eHP DeepSee, Spectra-Physics), a spinning-disk scanner with 100-μm-wide pinholes aligned on the Nipkow disk (CSU-MPϕ100; Yokogawa Electric) (Shimozawa et al., 2013), an inverted microscope (Ti2-E, Nikon), water immersion objective lens (Plan Apo IR 40X, numerical aperture: 1.15, Nikon), an XY controller (Ti2-S-JS, Nikon), an autofocusing system (Ti2-N-NDM-P, Nikon), a stage incubator (STXG-TIZWX-SET, Tokai Hit), and an EM-CCD camera (iXon Ultra 897, Andor Technology), which were controlled by the NIS-Elements software (Nikon). Time-lapse imaging of astrocytes was conducted over 90 s with 100-ms temporal resolutions. The oscillating wavelength of the Ti-Sa laser light was selected as 950-nm optimum for GCaMP6f excitation. Cells were perfused continuously at 37°C with ACSF. Aβ dimers and P2Y1 receptor antagonist (MRS2179) (ab120414, Abcam) were added using the perfusion system (flow rate 150 μl/min). Ca^{2+} imaging was performed after complete replacement of the solution in the recording dish. Astrocytes without any $[Ca^{2+}]_i$ changes or those with bright fluorescence due to a sign of cell death were excluded from the analysis.

Quantitative analysis of Ca^{2+} signals in astrocytes

Raw images were smoothed with a median filter (radius = 3.0 pixel) using the Fiji software (Schindelin et al., 2012), and the average intensity of the extracellular region was subtracted from the smoothed image as a background fluorescence. The cell boundary was semi-manually determined based on the fluorescence images of GCaMP6f. Briefly, a binary image was generated from the average image using the MinError method for image thresholding. Any areas where the outline could not be accurately reproduced were manually corrected. For the quantitative analysis of $[Ca^{2+}]_i$ elevations, we used the Astrocyte Quantification Analysis (AQuA) program of MATLAB (Mathworks) version developed based on an event-based machine-learning model (Wang et al., 2019). The $[Ca^{2+}]_i$ event occupancy was calculated by measuring the total area of $[Ca^{2+}]_i$ elevations divided by the area within the cell boundary. All AQuA parameters used in this study are presented in Table 1. To generate the two-dimensional map for the initiation point of $[Ca^{2+}]_i$ elevations in each experiment, the output data of AQuA analysis were used for further additional analysis. The total area of all $[Ca^{2+}]_i$ elevations throughout the Ca^{2+} imaging was extracted from the AQuA output and mapped as a binary image. The centroid of the earliest regions of each $[Ca^{2+}]_i$ elevation were calculated as average coordinates. The calculated centroids were mapped as cross-haired markers. These analyses were conducted using a custom MATLAB script.

Statistics

Statistical analyses were performed using Excel (Microsoft) and Origin (Origin Lab). Paired or unpaired t-tests were used for comparing two dependent and independent group means, respectively. Repeated one-way ANOVA with a post-hoc Holm–Bonferroni post-test was used to validate the Aβ dimers and drug effects when paired multiple group data were compared.

Results

Quantification analysis of spontaneous $[Ca^{2+}]_i$ elevations in cultured astrocytes

To visualize astrocytic $[Ca^{2+}]_i$ elevations with high spatial and temporal resolution, I used the high-speed low-invasive two-photon excitation spinning-disk confocal microscopy (Otomo et al., 2015; Otomo et al., 2020) and expressed the genetically-encoded Ca^{2+} probe, GCaMP6f, in the cytosol of primary cultured astrocytes. Diverse spontaneous $[Ca^{2+}]_i$ elevations were observed in different regions of astrocytes, as illustrated in Fig.1A. For the quantitative analysis of $[Ca^{2+}]_i$ elevations, I used an event-based machine-learning model, the AQuA algorithm (Wang et al., 2019) (Fig. 1B). The key parameters that define $[Ca^{2+}]_i$ elevations, such as amplitude ($\Delta F/F_0$), duration time (full-width half-maximum), area, and frequency, were extracted using the AQuA algorithm. No significant correlations were found either between "amplitude and duration" or "duration time and size of $[Ca^{2+}]_i$ elevations" ($r = 0.19$, $r = 0.26$) (Figs. 1C, D). The results suggest that the duration is not dependent on the area and amplitude of the $[Ca^{2+}]_i$ elevations. The histograms of duration and area revealed that the $[Ca^{2+}]_i$ elevations in astrocytes exhibited a continuous rather than a bimodal distribution (Figs. 1E, F). Therefore, I adopted a criterion in which 50% of the total $[Ca^{2+}]_i$ elevations defined the condition as fast and microdomain. The AQuA analysis for spontaneous astrocytic $[Ca^{2+}]_i$ elevations revealed that 50% of the astrocytic $[Ca^{2+}]_i$ elevations had a duration time of 0.5 s, and the area of that 50% of the $[Ca^{2+}]_i$ elevations was <35 μm^2. On the basis of these results, I classified the patterns of $[Ca^{2+}]_i$ elevations into four categories as follows: “fast-microdomain” (≤0.5 s, ≤35 μm^2), “slow-microdomain” (>0.5 s, ≤35 μm^2), “fast-region” (≤0.5 s, >35 μm^2), and “slow-region” (>0.5 s, >35 μm^2) (Fig. 1G). The definition of fast-microdomain was generally comparable to a previous study (Santello et al., 2011).

Effect of lower concentrations of Aβ dimers on $[Ca^{2+}]_i$ elevations astrocytes

To ensure the stability and continuity of Ca^{2+} recordings under my experimental conditions, I administered twice the highest concentration of organic solvent (1% DMSO) used in this study and monitored spontaneous $[Ca^{2+}]_i$ elevations (Fig. 2A). I compared the $[Ca^{2+}]_i$ event occupancy relative to cell area during pretreatment and DMSO administration and observed no significant differences (Figs. 2B and C). I also compared the frequency and amplitude of all four categories of $[Ca^{2+}]_i$ elevations (fast-microdomain, slow-microdomain, fast-region, and slow-region). Although the sites of $[Ca^{2+}]_i$ elevations in astrocytes changed from time to time during the recording, no significant differences were observed in any categories of $[Ca^{2+}]_i$ elevations (Figs. 2D and E).

Next, I systematically administered different concentrations of Aβ dimers (50 nM, 200 nM, 500 nM, 2 μM, and 5 μM) and analyzed the event occupancy, frequency, and amplitude in all four categories. A recent study showed that 500 nM Aβ dimers induced $[Ca^{2+}]_i$ elevation in neurons (Zott et al., 2019). Therefore, we investigated the effect of five concentrations of Aβ dimers at lower and higher concentrations of 500 nM in astrocytes. Representative examples and a statistical comparison are illustrated in Fig. 9, and the results of individual experiments are depicted in Figures 3–7.

Low concentrations (50, 200 nM) of Aβ dimers exerted no significant effect on the $[Ca^{2+}]_i$ event occupancy (Figs. 3BC, 4BC) as well as on the frequency and amplitude in all four categories (Figs. 3D and E, 4D and E). I concluded that <200 nM Aβ dimers exerted no detectable effect on spontaneous $[Ca^{2+}]_i$ elevations.

Effect of higher concentrations of Aβ dimers on $[Ca^{2+}]_i$ elevations in astrocytes

I further explored the effect of higher concentrations of Aβ dimers on $[Ca^{2+}]_i$ elevations. At 500 nM, 2 μM, and 5 μM concentrations (Figs. 5–7), there was a significant increase in the $[Ca^{2+}]_i$ event occupancy (Figs. 5BC, 6BC, 7BC) as well as in the frequency of fast-microdomain, slow-microdomain, slow-region $[Ca^{2+}]_i$ elevations (Figs. 5DE, 6E, 7DE). On the other hands, there was no difference in the proportion of fast $[Ca^{2+}]_i$ elevations between before application, Aβ dimers application, and washout(Fig. 8). At 5 μM, Aβ dimers further increased the amplitude of slow-region $[Ca^{2+}]_i$ elevations (Fig. 7E). At high concentrations of Aβ dimers (2 μM, 5 μM), the effects on $[Ca^{2+}]_i$ elevations were not reversible after washout (Figs. 6, 7D, E), suggesting that Aβ dimers tightly bound to the target molecules and irreversibly altered $[Ca^{2+}]_i$ signaling in astrocytes.

The summary graphs in Fig. 9 reveal that Aβ dimers exerted dose dependent effects on the event occupancy and frequency of $[Ca^{2+}]_i$ elevations. In addition, Aβ dimers exerted effects on the amplitude of slow-region $[Ca^{2+}]_i$ elevations. The effects of Aβ dimers on $[Ca^{2+}]_i$ elevations were not evident at 200 nM but became significant at >500 nM, indicating a threshold-like response of Aβ dimers on astrocytes (Fig. 9). In most of the categories (fast-microdomain, slow-microdomain, slow-region), the frequency, but not the amplitude, increased significantly with the concentration of Aβ dimers (Figs. 9C and D). 500 nM, 2 μM and 5 μM Aβ dimers altered the frequency of fast-region $[Ca^{2+}]_i$ elevations over a wide range. These findings indicate that Aβ dimers dose-dependently increased the $[Ca^{2+}]_i$ elevations in astrocytes. The data for all figures and statistical results are summarized in Table2-8.

Aβ dimers-induced $[Ca^{2+}]_i$ elevations are mediated by P2Y1 receptor activation

I next investigated the mechanism of Aβ dimers-induced $[Ca^{2+}]_i$ elevations. Previous studies have demonstrated that, under physiological conditions, fast-microdomain $[Ca^{2+}]_i$ elevations involve the activation of purinergic G protein-coupled P2Y1 receptors (Santello et al., 2011; Shigetomi et al., 2018). To examine whether Aβ dimers-induced $[Ca^{2+}]_i$ elevations are mediated by P2Y1 receptors, I analyzed $[Ca^{2+}]_i$ elevations in the presence of the P2Y1 receptor antagonist MRS2179 (20 μM) at an effective concentration of Aβ dimers of 500 nM (Fig. 10A). I observed that the event occupancy, frequency, and amplitude of $[Ca^{2+}]_i$ elevations remained unaffected by Aβ dimers administration in the presence of MRS2179 (Figs. 10B–E). These findings suggest that Aβ dimers-induced $[Ca^{2+}]_i$ elevations are mediated by signaling involving the activation of the P2Y1 receptor.

Discussion

Aβ dimers-induced alteration of fast-microdomain $[Ca^{2+}]_i$ elevations in astrocytes

I visualized Aβ dimers-induced alteration of $[Ca^{2+}]_i$ elevations in primary cultured astrocytes with high spatial and temporal resolution. I found that >70% of the spontaneous $[Ca^{2+}]_i$ elevations in the astrocytes had a duration of <1 s (Fig. 1C). Because the speed of Ca^{2+} imaging in previous studies was <1 Hz (Talantova et al., 2013; Pham et al., 2021; Shah et al., 2022), it is possible that most of the $[Ca^{2+}]_i$ elevations were below detectable levels.

It has been reported that Ca^{2+} microdomains in astrocytes reflect neuronal activity (Di Castro et al., 2011; Bindocci et al., 2017). Under experimental conditions where both neurons and astrocytes are present and communicate with each other, such as in brain slices or *in vivo*, it is difficult to distinguish which cell type the drug is acting on. I used primary cultured astrocytes as a simple model and analyzed the effects of Aβ dimers without considering the interaction with neurons. To the best of my knowledge, this is the first demonstration of the quantitative analysis of Aβ dimers acting directly on astrocytes.

Mechanistic insight into the site of action of Aβ dimers in astrocytes

I found that Aβ dimers at >500 nM increased the frequency of $[Ca^{2+}]_i$ elevations in astrocytes. Although the mechanism and target site of Aβ dimers remain to be elucidated, my findings suggest that the number of Ca^{2+} channels activated by Aβ dimers is increased in the astrocyte. Under physiological conditions, elevated Ca^{2+} is either taken up into the endoplasmic reticulum (ER) via the sarcoplasmic reticulum Ca^{2+}-ATPase (SERCA) or pumped out of the cells via the sodium–calcium exchanger (NCX) on the plasma membrane. My results suggest that the balance of Ca^{2+} influx and efflux is altered by Aβ dimers. A higher concentration of Aβ dimers of 5 μM further

increased the amplitude of $[Ca^{2+}]_i$ elevations. This may be because the fast $[Ca^{2+}]_i$ elevations were accumulated, causing a large and long-lasting $[Ca^{2+}]_i$ elevation that spread widely throughout the astrocyte.

Importantly, Aβ dimers-induced $[Ca^{2+}]_i$ elevations were inhibited by a P2Y1 receptor antagonist (Fig. 10). P2Y1 receptors are G protein-coupled receptors that produce IP3, which then causes the release of $[Ca^{2+}]_i$ elevations from the ER via IP3 receptors (Abbracchio et al., 2006). Hence, Aβ dimers-induced $[Ca^{2+}]_i$ elevations can be attributed to IP3-induced Ca^{2+} release (IICR). A previous study using HeLa cells reported that Ca^{2+} microdomains coincide with the localization of IP3 receptors (Thillaiappan et al., 2017). The astrocyte expresses all IP3R subtypes in the soma and its processes (Sherwood et al., 2021). The increased event occupancy (Figs. 5-7B, C) could be due to an increased number of IP3 receptor sites activated by Aβ dimers.

Identifying the key molecules involved in Aβ oligomers binding will be critical for drug development for AD treatment. Previous studies have reported that various receptor proteins selectively bind to distinct types of Aβ oligomer species (Jarosz-Griffiths et al., 2016). In neurons, Aβ dimers bind β2 adrenergic receptors (Wang et al., 2010). Whether Aβ oligomers bind directly to P2Y1 receptors or bind to another molecule to activate P2Y1R remains incompletely understood. It has been demonstrated that ATP release from CX hemichannels, a major pathway for ATP release from astrocytes, activates astrocyte P2Y1 receptors and induces $[Ca^{2+}]_i$ elevations (Torres et al., 2013). Aβ dimers may initiate ATP release from CX hemichannels and subsequently activate astrocytic P2Y1 receptors.

Spontaneous $[Ca^{2+}]_i$ elevations under physiological condition in astrocytes

In this study, I observed that astrocytes exhibit four patterns of $[Ca^{2+}]_i$ elevation in astrocytes (Fig. 1G). These distinct patterns could result from the mechanisms of Ca^{2+} release/uptake via the ER and

calcium buffering with calcium-binding proteins in the cytosol. For example, fast-microdomain $[Ca^{2+}]_i$ elevations could be generated by Ca^{2+} release from the ER (Di Castro et al., 2011), where locally released Ca^{2+} binds to calcium-binding proteins and/or is rapidly taken up into the ER. The regional $[Ca^{2+}]_i$ elevations could occur when large amounts of Ca^{2+} are released from multiple release sites or when Ca^{2+} is released from the ER for prolonged period due to saturation of Ca^{2+} with the calcium-binding proteins. The slow-microdomain $[Ca^{2+}]_i$ elevations may reflect prolonged and continuous release of local Ca^{2+} from the ER.

Visualization of spontaneous fast-microdomain $[Ca^{2+}]_i$ elevations in astrocytes

Several analysis programs such as GECIquant (Srinivasan et al. 2015), CaSCaDe (Agarwal et al., 2017), and AQuA have been proposed as techniques for analyzing the intricate $[Ca^{2+}]_i$ elevations in astrocytes (Lia et al. 2021). Among them, AQuA led to substantial advances in analysis of astrocytic $[Ca^{2+}]_i$ elevations (Liu et al. 2021). In the range of interest (ROI) -based approach such as GECI quant, CaSCaDe,-the lack of flexibility in the ROI, which does not change the shape or the position, poses a challenge to detecting of complex $[Ca^{2+}]_i$ elevations in astrocytes. On the other hand, AQuA was developed based on an event-based machine-learning model for analyzing huge data sets of the timelapse fluorescent images. As shown here, it enabled to clarify $[Ca^{2+}]_i$ elevations of ROI-violating factors more precisely -size variability, location variability and propagation. Since AQuA was capable for detecting fast $[Ca^{2+}]_i$ elevations with high resolution, such a machine-learning assisted approach for huge imaging data has great potential to significantly advance our understanding of the physiology and the molecular basis in astrocytes.

Future perspectives

Applying AQuA to calcium dynamics in primary cultured astrocytes, diverse $[Ca^{2+}]_i$ elevations such as fast-microdomain as well as slow-region were detected. Notably, 10% of all responses lasted less

than 0.2 seconds (Fig. 1C), which is detection limit of GCaMP6f (Chen et al., 2013). These results indicate the existence of $[Ca^{2+}]_i$ elevations with a duration of 0.2 seconds or less. The importance of more faster $[Ca^{2+}]_i$ elevations in relation to astrocytic functions remains unclear. Our microscopic technique enables visualization of such fast $[Ca^{2+}]_i$ elevations, and the development of faster-responding calcium probes will investigate the exploration of the physiological significance of these $[Ca^{2+}]_i$ elevations in astrocytes.

Large-scale drug screening will be required to identify the mechanism of action through which Aβ oligomers activate receptors. The primary culture of astrocytes used in this study allows evaluating the effects of drugs without considering the neuronal inputs. In future studies, brain slice or *in vivo* experiments are essential to determine the relationship between the effects of Aβ oligomers on astrocytes and dendritic spine loss.

Under physiological conditions, fast-microdomain $[Ca^{2+}]_i$ elevations in astrocytes might induce glutamate release (Santello et al., 2011). Moreover, a previous study has reported that 500 nM Aβ dimers increase extracellular glutamate concentrations (Zott et al., 2019). In this study, I found that the P2Y1 receptor pathway is involved in Aβ dimers-mediated fast-microdomain $[Ca^{2+}]_i$ elevations. It will be important to explore whether Aβ dimers actually enhance glutamate release from astrocytes and whether P2Y1 is involved in this pathway. This will be a key cellular signaling pathway in the very early stage of AD.

Acknowledgements

I am very grateful to Prof.Tomomi Nemoto for many valuable supports and helpful advice about the research contents and the writing of this article as the supervisor. I also thank Dr.Kohei Otomo at Juntendo University, for his technical advice about two-photon excitation spinning disk confocal microscopy.

I also thank the Genetically-Encoded Neuronal Indicator and Effector Project and the Janelia Farm Research Campus of the Howard Hughes Medical Institute for sharing the GCaMP6f constructs.

I would gratefully thank to the member of my thesis committee Prof.Hideji Murakoshi of Division of Section of Multiphoton Neuroimaging, National Institute for Physiological Sciences; Prof.Takaaki Sokabe of Division of Division of Cell Signaling, National Institute for Physiological Sciences; Prof.Toshiko Yamazawa of Department of Core Research Facilities, The Jikei University School of Medicine.

I sincerely thank Dr. Ryosuke Enoki, Dr.Hirokazu Ishii, Dr.Motosuke Tsutsumi and Dr.Kazushi Yamaguchi at Biophotonics Research Group, Exploratory Research Center on Life and Living Systems (ExCELLS), National Institutes of Natural Sciences for their valuable supports and helpful advice. I really thank all members of my laboratory, Dr. Lee Ming-Liang, Dr.Chang Ching-Pu, Dr. Mitsutoshi Ataka, Dr.Sota Hiro, Ms.Kana Tsuchiya, Ms. Ayaka Osamura, Ms.Miyoko Shimomura, Ms.Yuki Watakabe, Ms.Chiemi Hyodoh, Ms.Maki Watanabe, Ms.Miwa Kawachi and all alumni and alumnae. I deeply appreciate all of those who supported my research and daily life.

Reference

Agarwal, A., Wu, P., Hughes, E., Fukaya, M., Tischfield, M., Langseth, A. et al. (2017). Transient Opening of the Mitochondrial Permeability Transition Pore Induces Microdomain Calcium Transients in Astrocyte Processes. Neuron 93, 587-605. doi: 10.1016/j.neuron.2016.12.034

Alberdi, E., Wyssenbach, A., Alberdi, M., Sánchez-Gómez, M., Cavaliere, F., Rodríguez, J. et al. (2013). Ca2+-dependent endoplasmic reticulum stress correlates with astrogliosis in oligomeric amyloid β-treated astrocytes and in a model of Alzheimer's disease. Aging Cell 12, 292-302. doi: 10.1111/acel.12054

Bazargani, N., and Attwell, D. (2016). Astrocyte calcium signaling: The third wave. Nat. Neurosci. 19, 182-189. doi: 10.1038/nn.4201

Ben Haim, L., and Rowitch, D.H. (2017). Functional diversity of astrocytes in neural circuit regulation. Nat. Rev. Neurosci. 18, 31-41. doi: 10.1038/nrn.2016.159

Bindocci, E., Savtchouk, I., Liaudet, N., Becker, D., Carriero, G., and Volterra, A. (2017). Three-dimensional Ca2+ imaging advances understanding of astrocyte biology. Science (1979) 356. doi: 10.1126/science.aai8185

Chen, G.F., Xu, T.H., Yan, Y., Zhou, Y.R., Jiang, Y., Melcher, K., et al. (2017). Amyloid beta: Structure, biology and structure-based therapeutic development. Acta Pharmacol. Sin. 38, 1205-1235. doi: 10.1038/aps.2017.28

Chen, T., Wardill, T., Sun, Y., Pulver, S., Renninger, S., Baohan, A., et al. (2013). Ultrasensitive fluorescent proteins for imaging neuronal activity. Nature (7458) 499. doi: 10.1038/nature12354

Cuellar-Santoyo, A.O., Ruiz-Rodríguez, V.M., Mares-Barbosa, T.B., Patrón-Soberano, A., Howe, A.G., Portales-Pérez, D.P., et al. (2022). Revealing the contribution of astrocytes to glutamatergic neuronal transmission. Front. Cell Neurosci. 16, 1037641. doi: 10.3389/fncel.2022.1037641

Di Castro, M.A., Chuquet, J., Liaudet, N., Bhaukaurally, K., Santello, M., Bouvier, D., et al. (2011). Local Ca2+ detection and modulation of synaptic release by astrocytes. Nat. Neurosci. 14, 1276-1284. doi: 10.1038/nn.2929

Ding, F., Liang, S., Li, R., Yang, Z., He, Y., Yang, S., et al. (2022). Astrocytes exhibit diverse Ca2+ changes at subcellular domains during brain aging. Front. Aging Neurosci. 14, 1029533. doi: 10.3389/fnagi.2022.1029533

lchihara, A., Tanaami, T., lsozaki, K., Sugiyama, Y., Kosugi, Y., Mikuriya, K., et al. (1996). High-Speed Confocal Fluorescence Microscopy Using a Nipkow Scanner with Microlenses for 3-D Imaging of Single Fluorescent Molecule in Real Time. Bioimages. 4, 57-62. doi: 10.11169/bioimages.4.57

Jarosz-Griffiths, H.H., Noble, E., Rushworth, J.V., and Hooper, N.M. (2016). Amyloid-β receptors: The good, the bad, and the prion protein. J. Biol. Chem. 291, 3174-3183. doi: 10.1074/jbc.R115.702704

Kamada, T., Otomo, K., Murata, T., Nakata, K., Hiruma, S., Uehara, R., et al. (2022). Low-invasive 5D visualization of mitotic progression by two-photon excitation spinning-disk confocal microscopy. Sci. Rep. 12, 809. doi: 10.1038/s41598-021-04543-7

Kawano, H., Oyabu, K., Yamamoto, H., Eto, K., Adaniya, Y., Kubota, K., et al. (2017). Astrocytes with previous chronic exposure to amyloid β-peptide fragment 1–40 suppress excitatory synaptic transmission. J. Neurochem. 143, 624-634. doi: 10.1111/jnc.14247

Lakowics, J. (2006). Multiphoton Excitation and Microscopy. Principles of Fluorescence Spectroscopy 607-621. doi:10.1007/978-0-387-46312-4

Lia, A., Henriques, V., Zonta, M., Chiavegato, A., Carmignoto, G., Gómez-Gonzalo, M., et al. (2021). Calcium Signals in Astrocyte Microdomains, a Decade of Great Advances. Front. Neurosci. 15. doi: 10.3389/fncel.2021.673433

Otomo, K., Goto, A., Yamanaka, Y., Hori, T., Nakayama, H., and Nemoto, T. (2020). High-peak-power 918-nm laser light source based two-photon spinning-disk microscopy for green fluorophores. Biochem. Biophys. Res. Commun. 529, 238-242. doi: 10.1016/j.bbrc.2020.05.213

Otomo, K., Hibi, T., Murata, T., Watanabe, H., Kawakami, R., Nakayama, H., et al. (2015). Multi-point scanning two-photon excitation microscopy by utilising a high-peak-power 1042-nm laser. Anal. Sci. 31, 307-313. Doi: 10.2116/analsci.31.307

Paumier A, Boisseau S, Pernet-Gallay K, Buisson A, Albrieux M (2021). Astrocyte-neuron interplay is critical for Alzheimer's disease pathogenesis and is rescued by TRPA1 channel blockade. Brain. 145, 1. doi: 10.1101/2021.03.29.437466

Pham, C., Hérault, K., Oheim, M., Maldera, S., Vialou, V., Cauli, B., et al. (2021). Astrocytes respond to a neurotoxic Aβ fragment with state-dependent Ca2+ alteration and multiphasic transmitter release. Acta Neuropathol. Commun. 9, 44. doi: 10.1186/s40478-021-01146-1

Rose, C.R., Felix, L., Zeug, A., Dietrich, D., Reiner, A., and Henneberger, C. (2017). Astroglial glutamate signaling and uptake in the hippocampus. Front. Mol. Neurosci. 10, 451. doi: 10.3389/fnmol.2017.00451

Santello, M., Bezzi, P., and Volterra, A. (2011). TNFα controls glutamatergic gliotransmission in the hippocampal dentate gyrus. Neuron 69, 988-1001. doi: 10.1016/j.neuron.2011.02.003

Schindelin, J., Arganda-Carreras, I., Frise, E., Kaynig, V., Longair, M., Pietzsch, T., et al. (2012). Fiji: An open-source platform for biological-image analysis. Nat. Methods 9, 676-682. doi: 10.1038/nmeth.2019

Semyanov, A., Henneberger, C., and Agarwal, A. (2020). Making sense of astrocytic calcium signals — From acquisition to interpretation. Nat. Rev. Neurosci. 21, 551-564. doi: 10.1038/s41583-020-0361-8

Shah, D., Gsell, W., Wahis, J., Luckett, E.S., Jamoulle, T., Vermaercke, B., et al. (2022). Astrocyte calcium dysfunction causes early network hyperactivity in Alzheimer's disease. Cell Rep. 40, 111280. doi: 10.1016/j.celrep.2022.111280

Shankar, G.M., Li, S., Mehta, T.H., Garcia-Munoz, A., Shepardson, N.E., Smith, I., et al. (2008). Amyloid-β protein dimers isolated directly from Alzheimer's brains impair synaptic plasticity and memory. Nat. Med. 14, 837-842. doi: 10.1038/nm1782

Sherwood, M.W., Arizono, M., Panatier, A., Mikoshiba, K., and Oliet, S.H.R. (2021). Astrocytic IP3Rs: Beyond IP3R2. Front Cell Neurosci 15, 695817. doi: 10.3389/fncel.2021.695817

Shigetomi, E., Hirayama, Y.J., Ikenaka, K., Tanaka, K.F., and Koizumi, S. (2018). Role of purinergic receptor P2Y1 in spatiotemporal Ca 2+ dynamics in astrocytes. J. Neurosci. 38, 1383-1395. doi: 10.1523/JNEUROSCI.2625-17.2017

Shimozawa, T., Yamagata, K., Kondo, T., Hayashi, S., Shitamukai, A., Konno, D., et al. (2013). Improving spinning disk confocal microscopy by preventing pinhole cross-talk for intravital imaging. Proc. Natl. Acad. Sci. U. S. A. 110, 3399-3404. doi: 10.1073/pnas.1216696110

Srinivasan, R., Huang, B., Venugopal, S., Johnston, A., Chai, H., Zeng, H., et al. (2015). Ca2+ signaling in astrocytes from Ip3r2 -/- mice in brain slices and during startle responses in vivo. Nat Neurosci. 18, 708-717. doi: 10.1038/nn.4001

Talantova, M., Sanz-Blasco, S., Zhang, X., Xia, P., Akhtar, M.W., Okamoto, S.I., et al. (2013). Aβ

induces astrocytic glutamate release, extrasynaptic NMDA receptor activation, and synaptic loss. Proc. Natl. Acad. Sci. U. S. A. 110, E2518-E2527. doi: 10.1073/pnas.1306832110

Thillaiappan, N.B., Chavda, A.P., Tovey, S.C., Prole, D.L., and Taylor, C.W. (2017). Ca2+ signals initiate at immobile IP3 receptors adjacent to ER-plasma membrane junctions. Nat. Commun. 8, 1505. doi: 10.1038/s41467-017-01644-8

Torres, A., Wang, F., Xu, Q., Fujita, T., Dobrowolski, R., Willecke, K., et al. (2012). Extracellular Ca 2+ acts as a mediator of communication from neurons to glia. Sci. Signal. 5, ra8-ra8

Wang, D., Govindaiah, G., Liu, R., De Arcangelis, V., Cox, C.L., and Xiang, Y.K. (2010). Binding of amyloid β peptide to β 2 adrenergic receptor induces PKA-dependent AMPA receptor hyperactivity. FASEB J. 24, 3511-3521. doi: 10.1096/fj.10-156661

Wang, Y., DelRosso, N.V., Vaidyanathan, T.V., Cahill, M.K., Reitman, M.E., Pittolo, S., et al. (2019). Accurate quantification of astrocyte and neurotransmitter fluorescence dynamics for single-cell and population-level physiology. Nat. Neurosci. 22, 1936-1944. doi: 10.1038/s41593-019-0492-2

Zott, B., Simon, M.M., Hong, W., Unger, F., Chen-Engerer, H.J., Frosch, M.P., et al. (2019). A vicious cycle of β amyloid−dependent neuronal hyperactivation. Science 365, 559-565. doi: 10.1126/science.aay0198

Figures and Tables

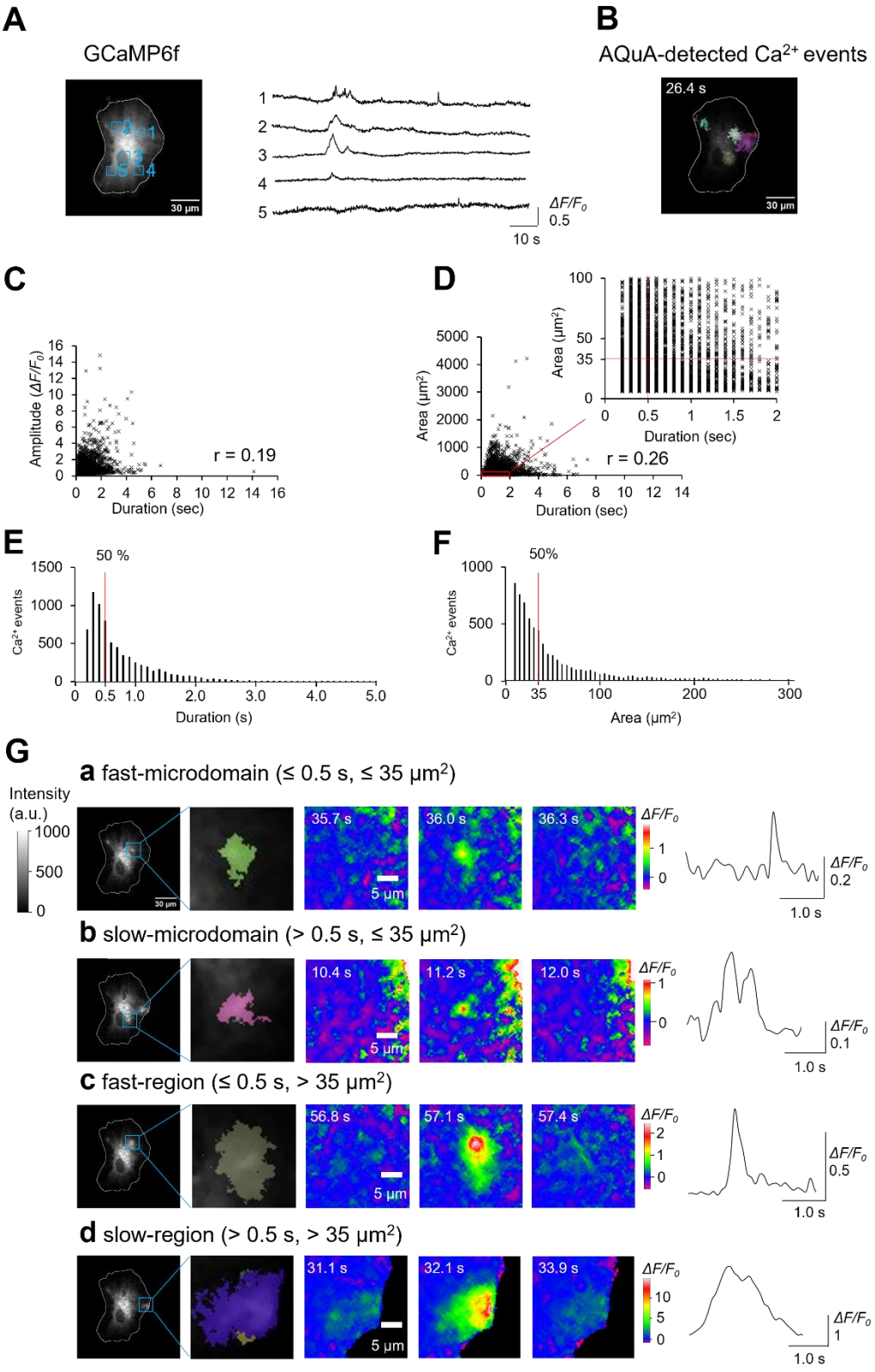

Figure 1. Classification of spatiotemporal $[Ca^{2+}]_i$ patterns in astrocytes

(A) Average time projection image (left) and $[Ca^{2+}]_i$ traces (right) of a representative astrocyte. The cell border is indicated by a white line. Boxed regions of interest (ROIs) correspond to the traces on the right. (B) Snapshot images of AQuA-detected $[Ca^{2+}]_i$ elevations. Each color in the bottom images represents individual AQuA-detected events. Colors are chosen randomly. (C) Histogram of duration time (s). (D) Histogram of area (μm^2). The red vertical line in (C) and (D) indicates 50% of total $[Ca^{2+}]_i$ elevations. (E) Representative images and traces of four categories of $[Ca^{2+}]_i$ elevations. The two left panels show AQuA-detected individual $[Ca^{2+}]_i$ elevations and their magnified images. The three pseudocolor images on the right correspond to the ROIs in the left. Traces of $[Ca^{2+}]_i$ elevations are illustrated on the right. The time is shown in the upper left corner of each pseudocolor image.

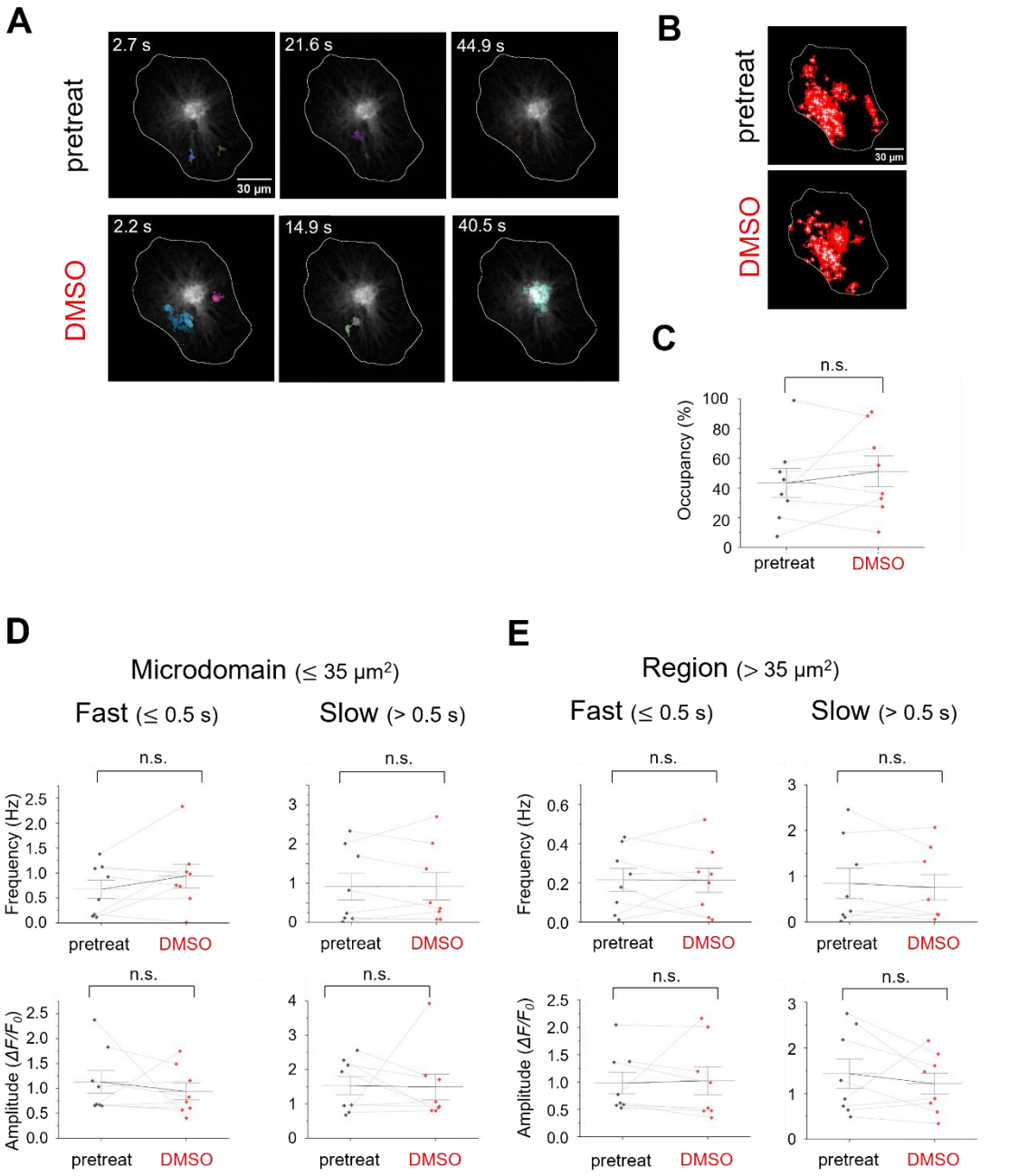

Figure 2. Effects of DMSO (1%) on $[Ca^{2+}]_i$ elevations in astrocytes

(A) Representative images of astrocytic $[Ca^{2+}]_i$ signals are shown with AQuA-detected events. Images of pretreat (top) and under DMSO application (bottom) are shown. The time is shown in the upper left corner of each image. The total acquisition time is 90 s for each condition. **(B)** Comparison of the area of $[Ca^{2+}]_i$ elevations in each condition. The two images on the left represent

the area of total of $[Ca^{2+}]_i$ elevations in the pretreat and DMSO application. The red area and the white cross indicate the area of $[Ca^{2+}]_i$ elevation and the center of gravity of individual $[Ca^{2+}]_i$ elevations, respectively. **(C)** Comparison of the event occupancy of $[Ca^{2+}]_i$ elevations between pretreat and DMSO application. **(D, E)** Frequencies (Hz) and amplitudes ($\Delta F/F_0$) of $[Ca^{2+}]_i$ elevations are compared between pretreat and DMSO application. Data are expressed as mean ± s.e.m. Paired t-test was used to compare differences (n = 8). Individual data and statistical results in the graphs are summarized in Table.

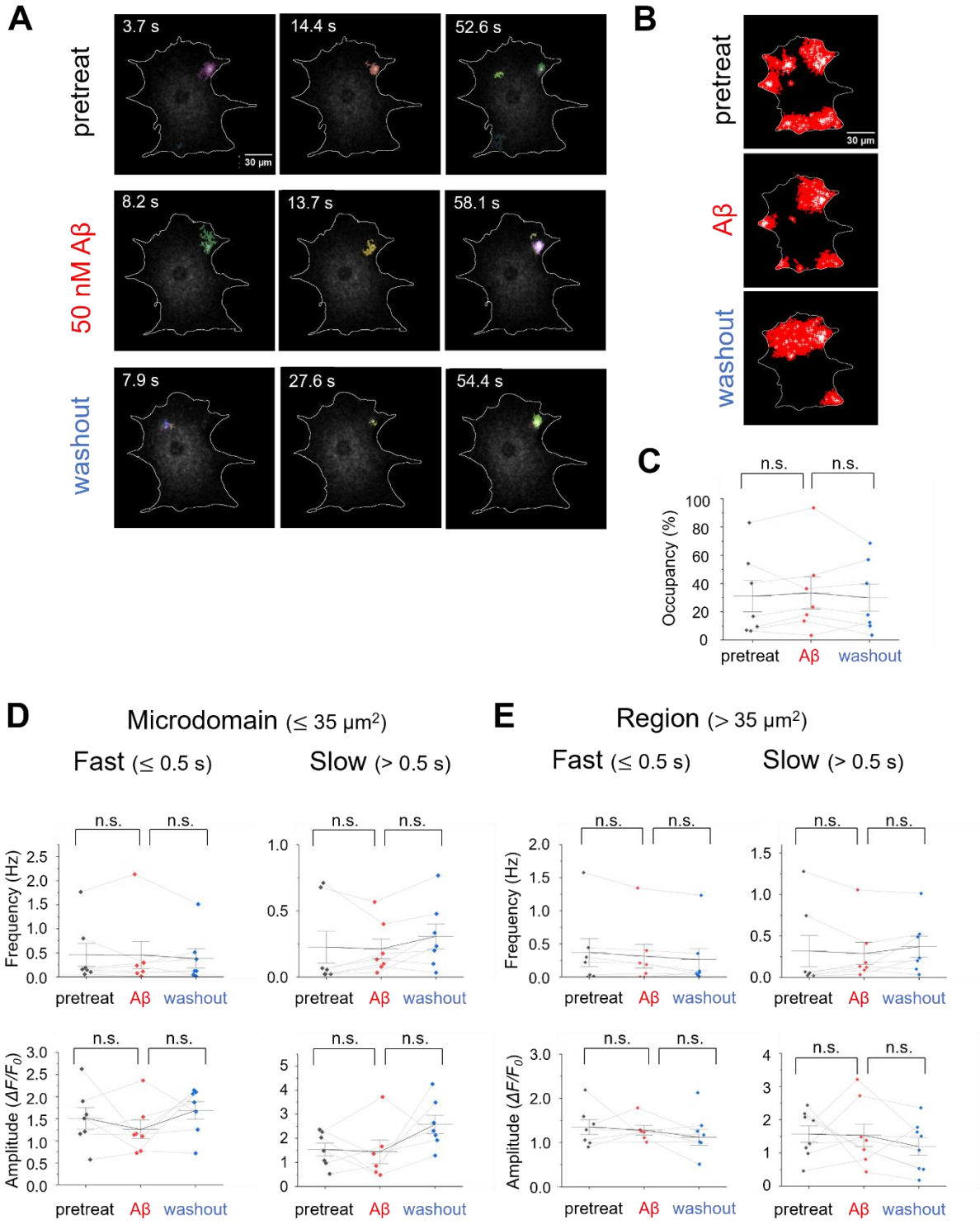

Figure 3. Effects of 50 nM Aβ dimers on $[Ca^{2+}]_i$ elevations in astrocytes

See figure legend in Fig. 3 (n = 7).

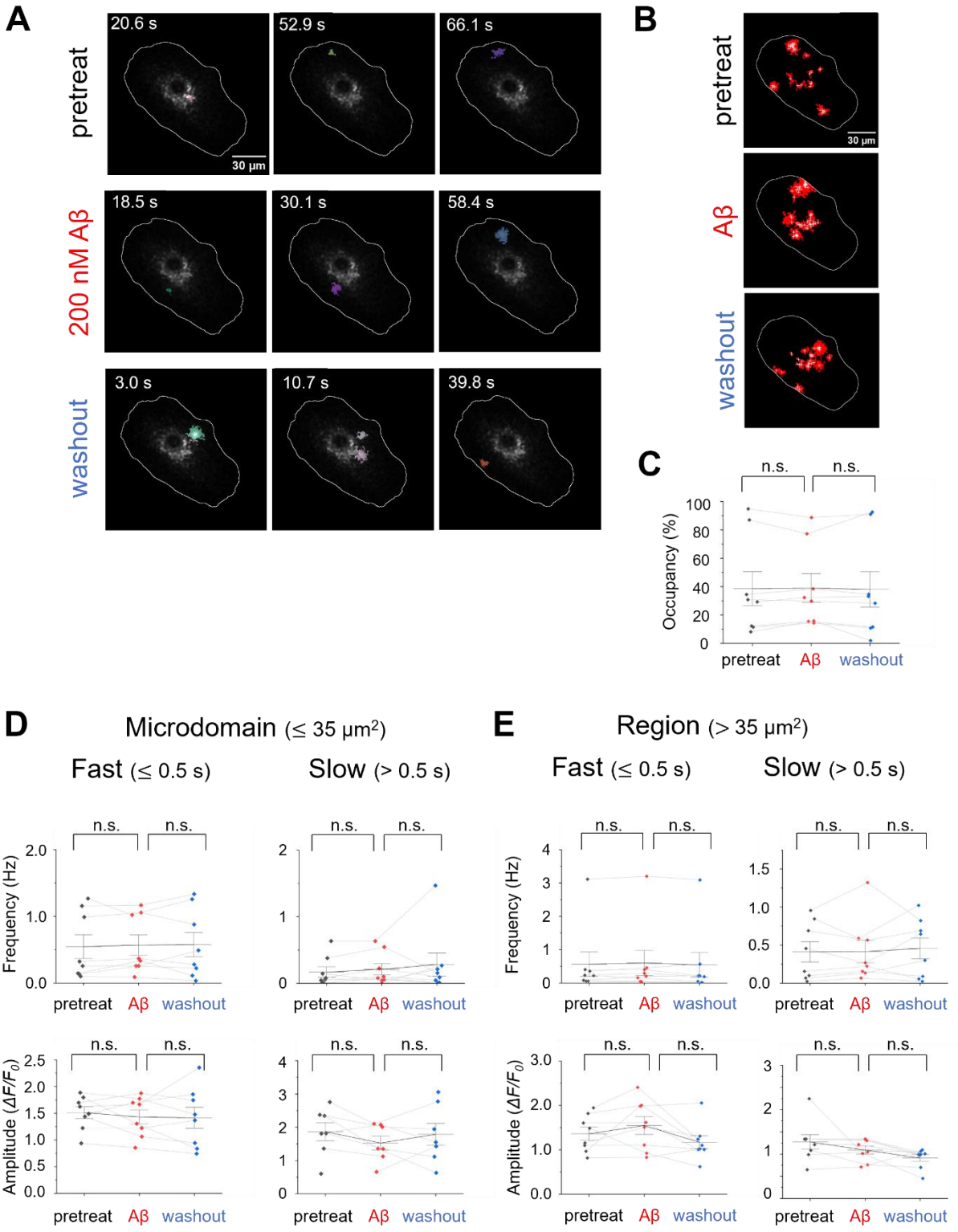

Figure 4. Effects of 200 nM Aβ dimers on $[Ca^{2+}]_i$ elevations in astrocytes

See figure legend in Fig. 3 (n = 8).

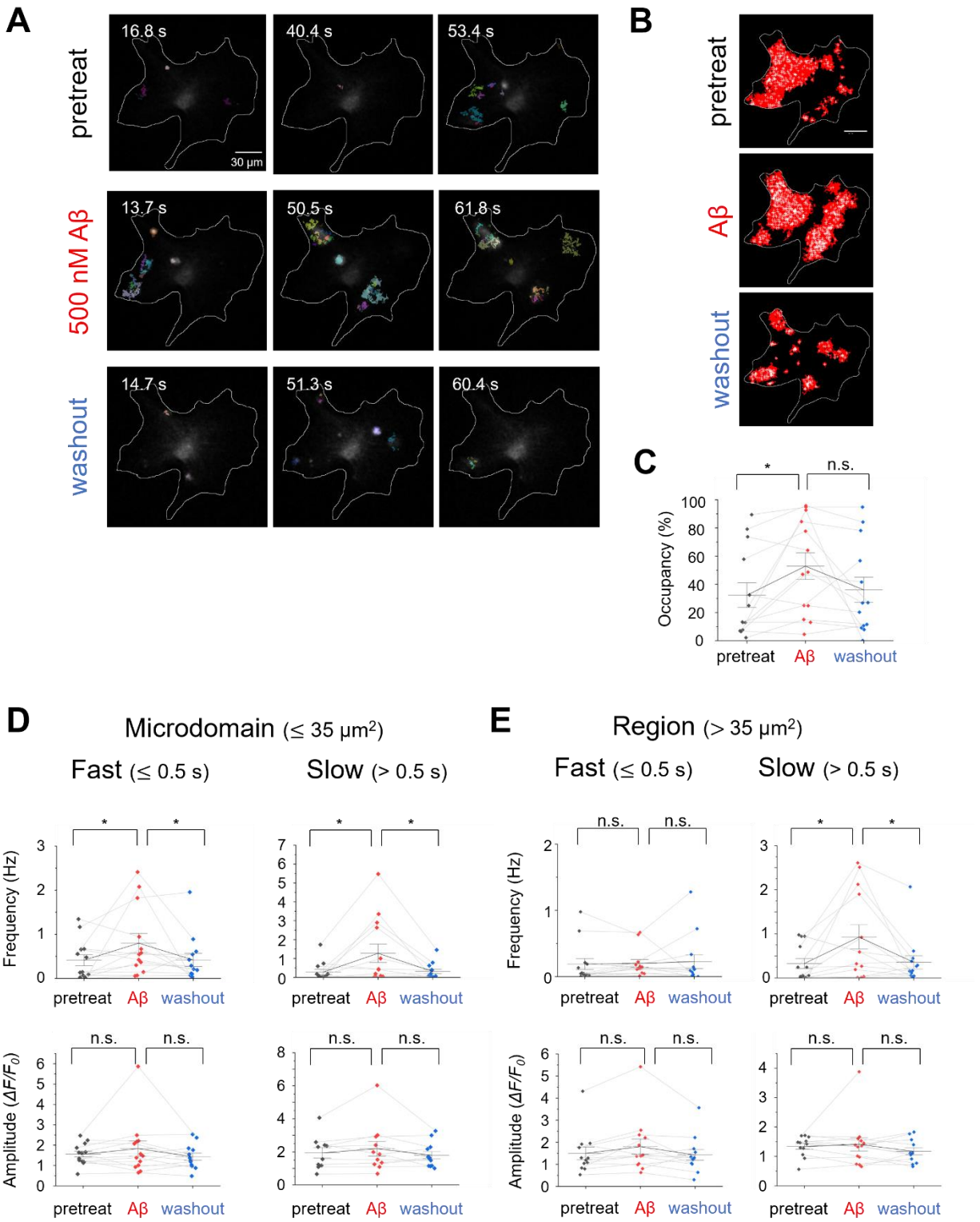

Figure 5. Effects of 500 nM Aβ dimers on $[Ca^{2+}]_i$ elevations in astrocytes

See figure legend in Fig. 3 (n = 13).

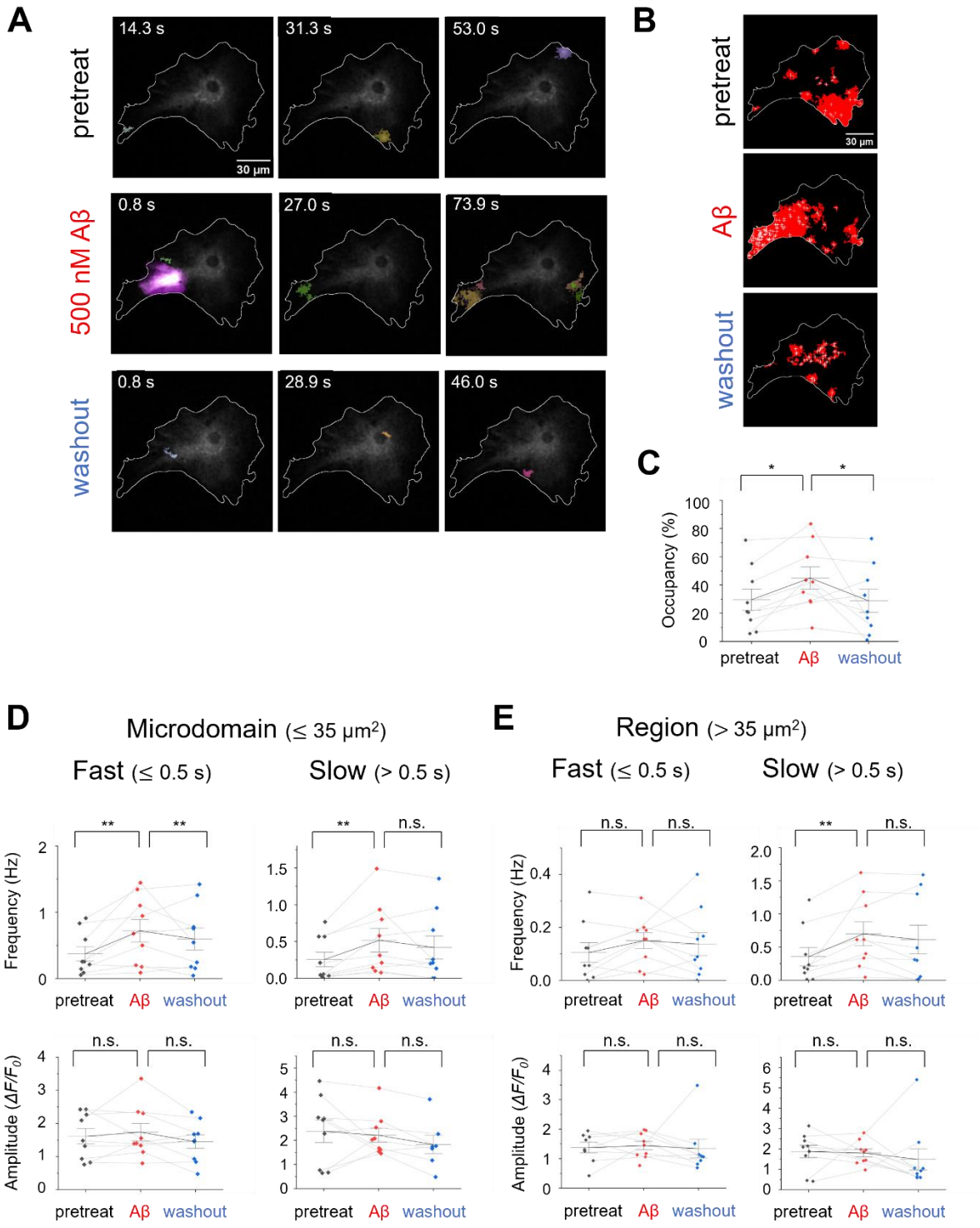

Figure 6. Effects of 2 μM Aβ dimers on $[Ca^{2+}]_i$ elevations in astrocytes

See figure legend in Fig. 3 (n = 9).

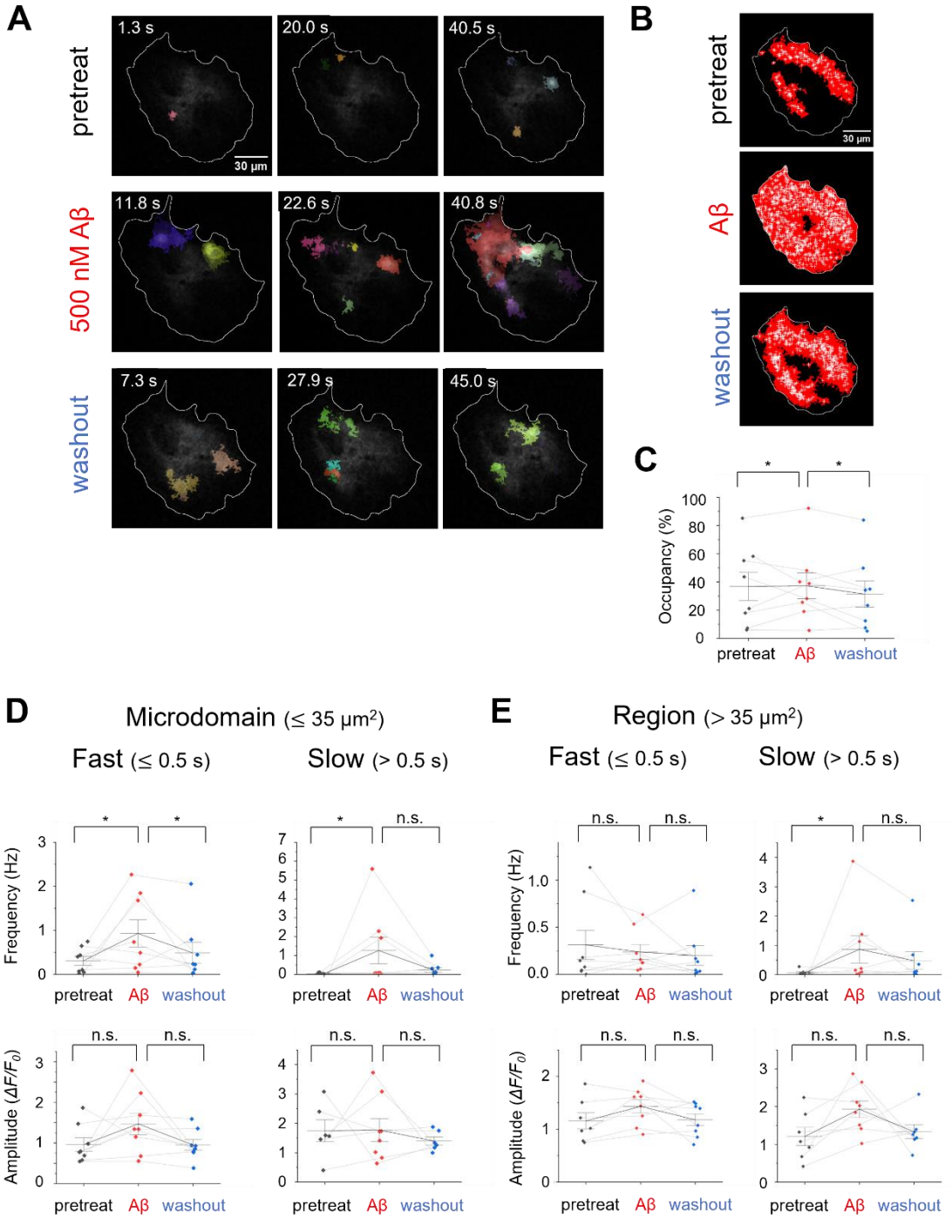

Figure 7. Effects of 5 μM Aβ dimers on $[Ca^{2+}]_i$ elevations in astrocytes

See figure legend in Fig. 3 (n = 8).

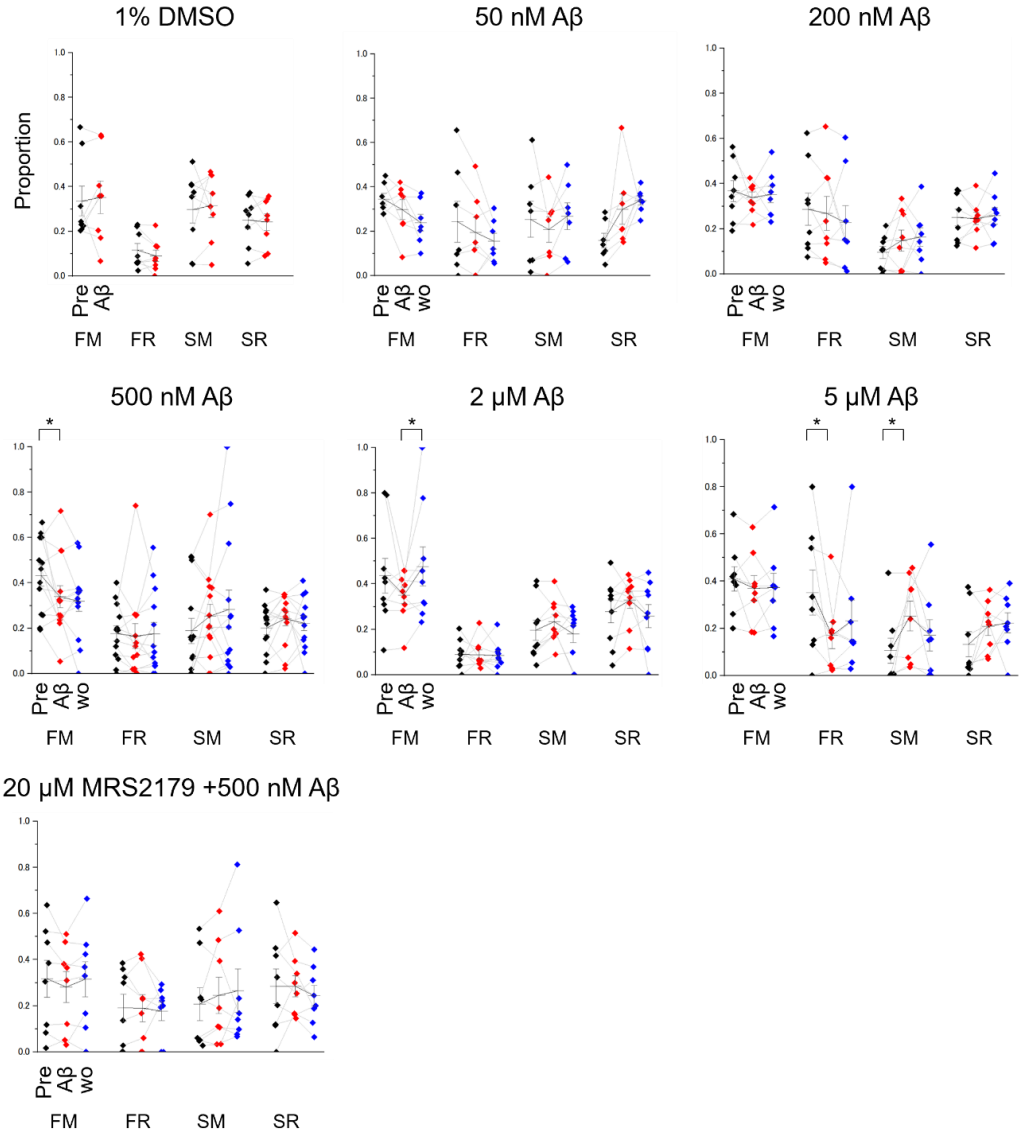

Figure 8. Comparison of proportion of each $[Ca^{2+}]_i$ elevations in each experimental condition between pretreat Aβ dimers application, and washout.

Abbreviations: FM, FR, SM, and SR are fast-microdomain, fast-region, slow-microdomain, slow-region, respectively. Data are presented as mean ± s.e.m. paired t-test (DMSO experiments) or one-way ANOVA with Holm-Bonferroni post-test was used to compare differences (DMSO: n=8, 50 nM Aβ: n=7 cells, 200 nM Aβ: n=8 cells, 500 nM Aβ: n=13 cells, 2 μM Aβ: n=9 cells, 5 μM Aβ: n=8 cells, 20 μM MRS2179+500 nM Aβ: n=8 cells, *: $p<0.05$, **: $p<0.01$).

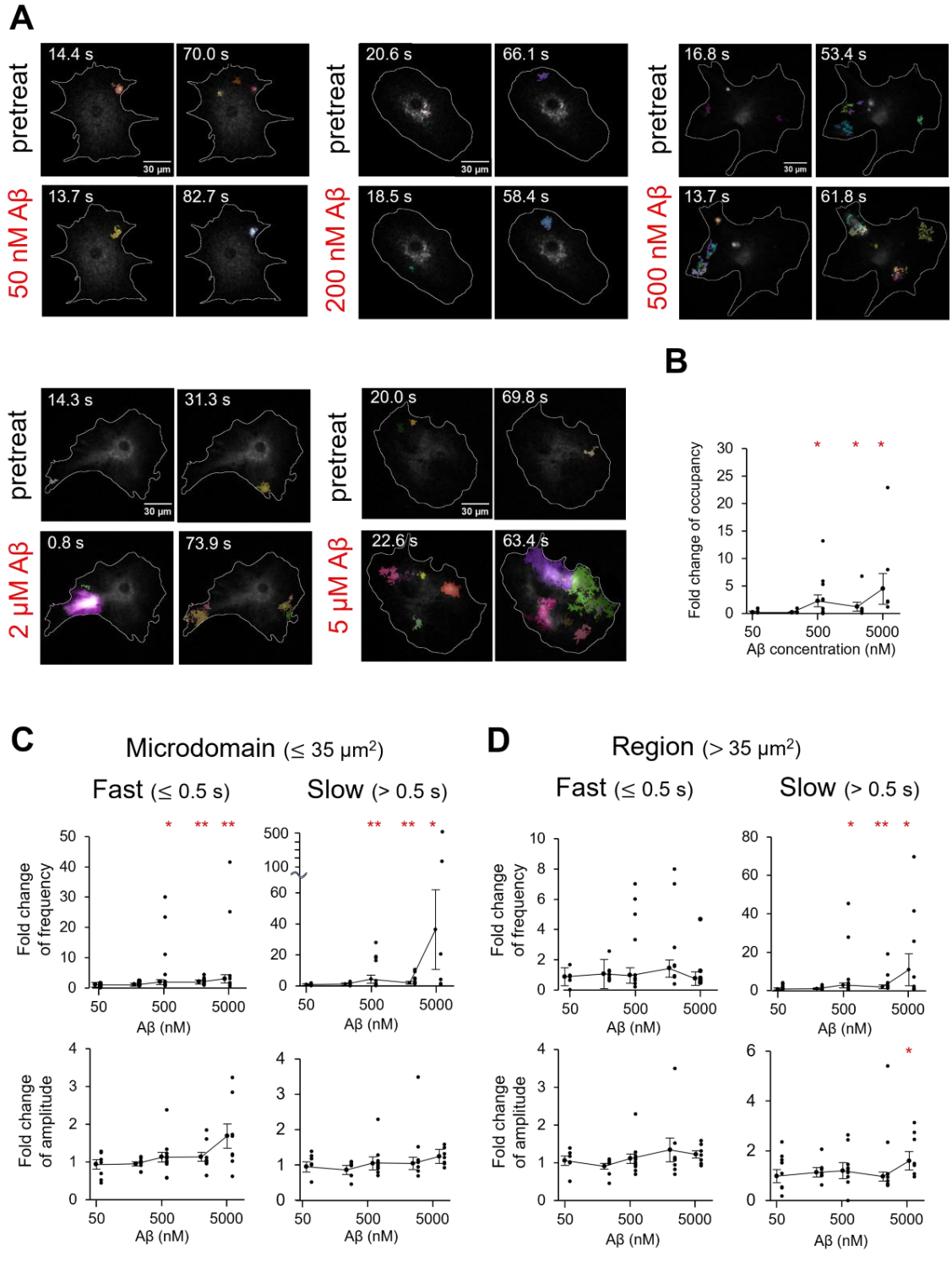

Figure 9. Dose-dependent effects of Aβ dimers on $[Ca^{2+}]_i$ elevations in astrocytes

(A) Representative images of astrocytic $[Ca^{2+}]_i$ elevations displayed with AQuA-detected events

(indicated by colored areas). The cell boundary is indicated by a white line. The left and right images are the 50-nM and 5-μM Aβ dimer exposure images, respectively. The top and bottom images are the pretreat and Aβ dimer applications, respectively. The time is shown in the upper left corner of each image. The total acquisition time is 90 s. (B) Fold change of Aβ dimer application on the event occupancy of $[Ca^{2+}]_i$ elevations (n = 8–13 cells per condition). (C) Dose-dependent changes in the effects of Aβ dimers on the frequency (top) and amplitude (bottom) of microdomain $[Ca^{2+}]_i$ elevations. The categories of fast and slow $[Ca^{2+}]_i$ elevations are depicted in the left and right row graphs. (D) Dose-dependent changes in the effects of Aβ dimers on the frequency (top) and amplitude (bottom) of region $[Ca^{2+}]_i$ elevations. The categories of fast and slow $[Ca^{2+}]_i$ elevations are depicted in the left and right row graphs. In the graphs, individual data (dots) and mean ± sem data are shown. One-way ANOVA with Holm–Bonferroni post-test was used to evaluate the difference. *: $p < 0.05$, **: $p < 0.01$ (50 nM: n = 7 cells, 200 nM: n = 8 cells, 500 nM: n = 13 cells, 2 μM: n = 9 cells, 5 μM: n = 8 cells). Individual data and statistical results in the graphs are summarized in Tables 2-8.

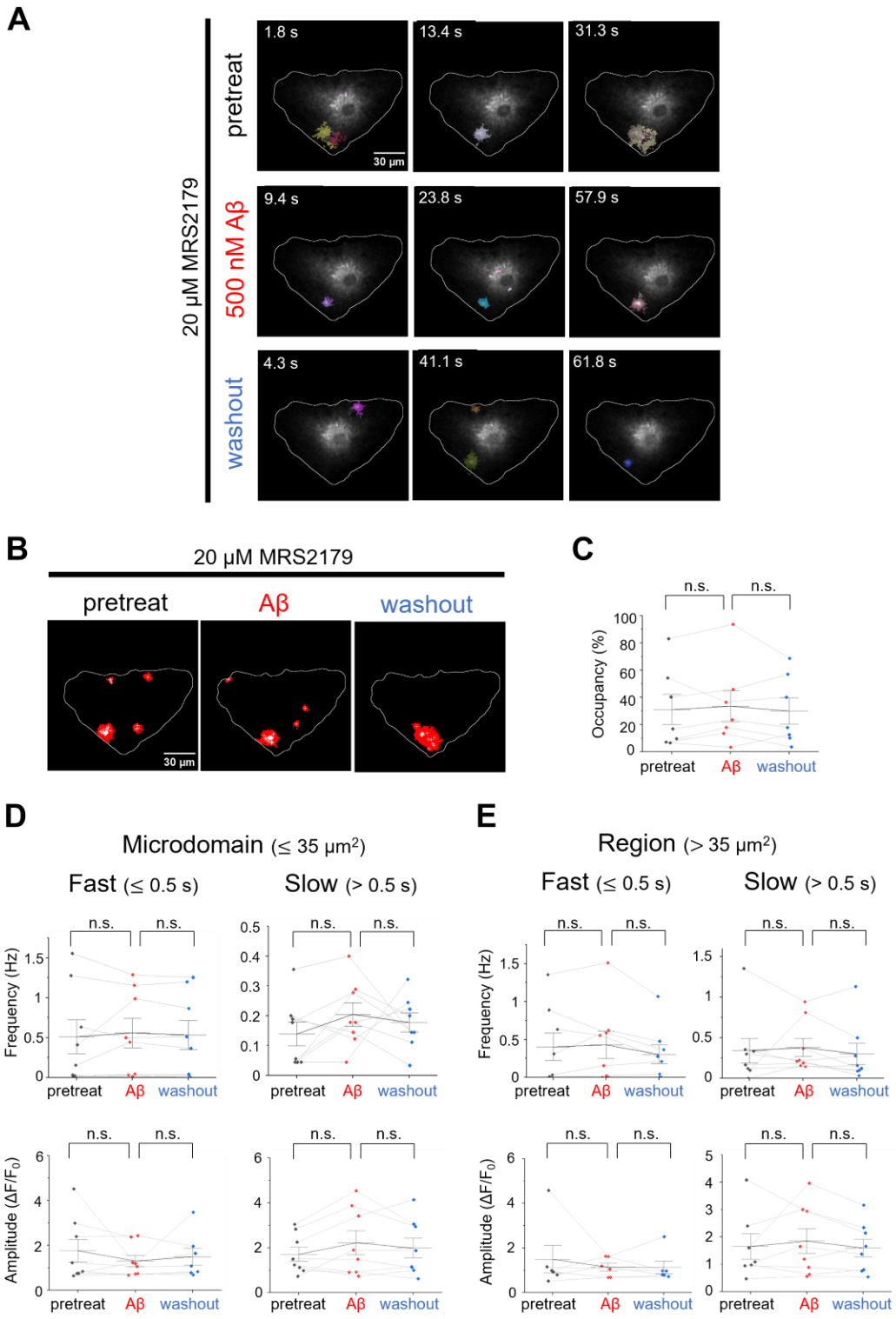

Figure 10. P2Y1 receptor antagonist inhibits Aβ dimers-induced $[Ca^{2+}]_i$ elevations in astrocytes

See figure legend in Fig. 3 (n = 8).

Table 1. AQuA parameters used to detect $[Ca^{2+}]_i$ events in astrocytes

Parameters	Value
Signal: intensity threshold	3
Signal: smoothing	0
Signal: minimum size	50 px
Voxel: temporal cut	2
Voxel: growing z	1
Event: rising time uncertainty	2
Event: slowest delay in propagation	2
Event: propagation smoothness	1
Clean: Z-score threshold	3

Table 2. Summary data of p-value, mean, and s.e.m as Figure 2

		Pre	Aβ
Area(Fig.2C)	Mean	0.43	0.51
	SEM	0.10	0.10
	P-value	0.38	

		Microdomain (Fig. 2D)			
		Fast		**Slow**	
		Pre	Aβ	Pre	Aβ
Frequency	Mean	0.67	0.90	0.91	0.91
	SEM	0.18	0.25	0.34	0.35
	P-value	0.47		0.47	
Amplitude	Mean	1.53	1.51	1.43	1.31
	SEM	0.27	0.38	0.32	0.28
	P-value	0.75		0.96	

		Region (Fig. 2E)			
		Fast		**Slow**	
		Pre	Aβ	Pre	Aβ
Frequency	Mean	0.22	0.21	0.84	0.75
	SEM	0.06	0.06	0.33	0.28
	P-value	0.95		0.84	
Amplitude	Mean	0.98	1.10	0.22	0.21
	SEM	0.19	0.28	0.06	0.06
	P-value	0.72		0.77	

Table 3. Summary data of p-value, mean, and s.e.m as Figure 3

		Pre	Aβ	Washout
Area(Fig.3C)	Mean	0.31	0.33	0.30
	SEM	0.11	0.11	0.10
	P-value	0.59		0.43

		Microdomain (Fig. 3D)					
		Fast			**Slow**		
		Pre	Aβ	Washout	Pre	Aβ	Washout
Frequency	Mean	0.46	0.45	0.38	0.21	0.17	0.19
	SEM	0.24	0.28	0.20	0.10	0.08	0.05
	P-value	0.94	0.50		0.65	0.65	
Amplitude	Mean	1.51	1.26	1.69	1.53	1.44	0.94
	SEM	0.24	0.21	0.20	0.27	0.49	0.36
	P-value	0.39	0.15		0.80	0.10	

		Region (Fig. 3E)					
		Fast			**Slow**		
		pre	Aβ	Washout	pre	Aβ	Washout
Frequency	Mean	0.37	0.31	0.26	0.32	0.29	0.37
	SEM	0.21	0.18	0.17	0.19	0.14	0.13
	P-value	0.19	0.23		0.71	0.30	
Amplitude	Mean	1.36	1.28	1.63	1.42	1.36	0.96
	SEM	0.20	0.13	0.28	0.28	0.34	0.31
	P-value	0.73	0.35		0.89	0.057	

Table 4. Summary data of p-value, mean, and s.e.m as Figure 4

		Pre	Aβ	Washout
Area(Fig.4C)	Mean	0.39	0.37	0.31
	SEM	0.10	0.09	0.09
	P-value	0.83		0.65

		Microdomain (Fig. 4D)					
		Fast			**Slow**		
		Pre	Aβ	Washout	pre	Aβ	Washout
Frequency	Mean	0.53	0.54	0.58	0.17	0.21	0.29
	SEM	0.18	0.15	0.18	0.08	0.09	0.17
	P-value	0.81	0.51		0.72	0.45	
Amplitude	Mean	1.47	1.40	1.41	1.36	1.54	1.45
	SEM	0.10	0.12	0.20	0.15	0.20	0.26
	P-value	0.59	0.92		0.40	0.45	

		Region (Fig. 4E)					
		Fast			**Slow**		
		pre	Aβ	Washout	pre	Aβ	Washout
Frequency	Mean	0.56	0.60	0.54	0.41	0.42	0.46
	SEM	0.37	0.38	0.37	0.13	0.15	0.13
	P-value	0.38	0.15		0.96	0.62	
Amplitude	Mean	1.27	1.09	1.47	1.36	1.55	1.45
	SEM	0.16	0.09	0.19	0.15	0.20	0.26
	P-value	0.40	0.10		0.34	0.63	

Table 5. Summary data of p-value, mean, and s.e.m as Figure 5

		Pre	Aβ	Washout
Area(Fig.5C)	Mean	0.32	0.53	0.36
	SEM	0.09	0.09	0.09
	P-value	0.022		0.057

		Microdomain (Fig. 5D)					
		Fast			**Slow**		
		Pre	Aβ	Washout	pre	Aβ	Washout
Frequency	Mean	0.42	0.81	0.43	0.28	1.28	0.31
	SEM	0.12	0.22	0.15	0.14	0.48	0.12
	P-value	0.045	0.049		0.006	0.008	
Amplitude	Mean	1.56	1.83	1.44	1.94	2.19	1.13
	SEM	0.14	0.37	0.18	0.32	0.44	0.30
	P-value	0.36	0.25		0.34	0.29	

		Region (Fig. 5E)					
		Fast			**Slow**		
		pre	Aβ	Washout	pre	Aβ	Washout
Frequency	Mean	0.19	0.20	0.22	0.33	0.93	0.35
	SEM	0.08	0.06	0.10	0.11	0.27	0.15
	P-value	0.88	0.73		0.011	0.015	
Amplitude	Mean	1.34	1.41	1.17	1.50	1.80	1.20
	SEM	0.10	0.23	0.12	0.29	0.34	0.32
	P-value	0.82	0.44		0.12	0.07	

Table 6. Summary data of p-value, mean, and s.e.m as Figure 6

		Pre	Aβ	Washout
Area(Fig.6C)	Mean	0.30	0.45	0.29
	SEM	0.08	0.08	0.08
	P-value	0.032	0.025	

		Microdomain (Fig. 6D)					
		Fast			**Slow**		
		Pre	Aβ	Washout	Pre	Aβ	Washout
Frequency	Mean	0.37	0.72	0.59	0.25	1.28	0.31
	SEM	0.11	0.17	0.17	0.10	0.48	0.12
	P-value	0.0045	0.25		0.0083	0.26	
Amplitude	Mean	1.61	1.74	1.37	2.37	2.21	1.81
	SEM	0.23	0.26	0.21	0.47	0.29	0.38
	P-value	0.48	0.054		0.99	0.66	

		Region (Fig. 6E)					
		Fast			**Slow**		
		Pre	Aβ	Washout	Pre	Aβ	Washout
Frequency	Mean	0.10	0.15	0.14	0.33	0.93	0.35
	SEM	0.04	0.03	0.04	0.11	0.27	0.15
	P-value	0.19	0.71		0.0047	0.42	
Amplitude	Mean	1.38	1.44	1.24	1.87	1.80	1.30
	SEM	0.18	0.15	0.14	0.31	0.19	0.18
	P-value	0.77	0.34		0.80	0.17	

Table 7. Summary data of p-value, mean, and s.e.m as Figure 7

		Pre	Aβ	Washout
Area(Fig.7C)	Mean	0.16	0.50	0.23
	SEM	0.04	0.14	0.07
	P-value	0.011		0.036

		Microdomain (Fig. 7D)					
		Fast			**Slow**		
		Pre	Aβ	Washout	Pre	Aβ	Washout
Frequency	Mean	0.31	0.93	0.49	0.037	1.27	0.24
	SEM	0.10	0.31	0.24	0.016	0.70	0.12
	P-value	0.0044	0.20		0.038	0.080	
Amplitude	Mean	0.96	1.47	0.95	1.75	1.77	1.40
	SEM	0.17	0.27	0.13	0.37	0.39	0.14
	P-value	0.47	0.42		0.50	0.41	

		Region (Fig. 7E)					
		Fast			**Slow**		
		Pre	Aβ	Washout	Pre	Aβ	Washout
Frequency	Mean	0.31	0.24	0.20	0.33	0.93	0.35
	SEM	0.15	0.79	0.10	0.11	0.27	0.15
	P-value	0.43	0.83		0.0045	0.37	
Amplitude	Mean	1.16	1.43	1.18	1.21	1.93	1.33
	SEM	0.15	0.12	0.11	0.24	0.22	0.19
	P-value	0.39	0.97		0.028	0.30	

Table 8. Summary data of p-value, mean, and s.e.m as Figure 10

		Pre	Aβ	Washout
Area (Fig.10C)	Mean	0.37	0.37	0.31
	SEM	0.10	0.09	0.09
	P-value	0.93		0.24

		Microdomain (Fig. 10D)					
		Fast			**Slow**		
		Pre	Aβ	Washout	pre	Aβ	Washout
Frequency	Mean	0.51	0.56	0.53	0.14	0.20	0.18
	SEM	0.21	0.19	0.18	0.04	0.04	0.03
	P-value	0.54	0.75		0.24	0.63	
Amplitude	Mean	1.75	1.30	1.49	1.71	2.21	1.98
	SEM	0.50	0.25	0.38	0.31	0.53	0.44
	P-value	0.25	0.81		0.08	0.41	

		Region (Fig. 10E)					
		Fast			**Slow**		
		pre	Aβ	Washout	pre	Aβ	Washout
Frequency	Mean	0.40	0.43	0.31	0.34	0.38	0.30
	SEM	0.18	0.18	0.13	0.15	0.11	0.13
	P-value	0.71	0.11		0.66	0.37	
Amplitude	Mean	1.49	1.13	1.12	1.65	1.85	1.60
	SEM	0.62	0.17	0.28	0.47	0.45	0.32
	P-value	0.39	0.97		0.30	0.43	